NANO · MICRO small
www.small-journal.com

Metastable Polymorphic Phases in Monolayer $TaTe_2$

Iolanda Di Bernardo, Joan Ripoll-Sau, Jose Angel Silva-Guillén, Fabian Calleja, Cosme G. Ayani, Rodolfo Miranda, Enric Canadell, Manuela Garnica,* and Amadeo L. Vázquez de Parga*

Polymorphic phases and collective phenomena—such as charge density waves (CDWs)—in transition metal dichalcogenides (TMDs) dictate the physical and electronic properties of the material. Most TMDs naturally occur in a single given phase, but the fine-tuning of growth conditions via methods such as molecular beam epitaxy (MBE) allows to unlock otherwise inaccessible polymorphic structures. Exploring and understanding the morphological and electronic properties of new phases of TMDs is an essential step to enable their exploitation in technological applications. Here, scanning tunneling microscopy (STM) is used to map MBE-grown monolayer (ML) $TaTe_2$. This work reports the first observation of the 1H polymorphic phase, coexisting with the 1T, and demonstrates that their relative coverage can be controlled by adjusting synthesis parameters. Several superperiodic structures, compatible with CDWs, are observed to coexist on the 1T phase. Finally, this work provides theoretical insight on the delicate balance between Te...Te and Ta–Ta interactions that dictates the stability of the different phases. The findings demonstrate that $TaTe_2$ is an ideal platform to investigate competing interactions, and indicate that accurate tuning of growth conditions is key to accessing metastable states in TMDs.

1. Introduction

Transition metal dichalcogenides (TMDs) have been intensively studied for the variety of physical properties they offer.[1,2] They are layered compounds with the formula MX_2, where M is a transition metal and X a chalcogen, characterized by weak, mostly van der Waals-like interactions between planes. According to the chalcogen coordination geometry within the unit cell, ultimately related to the *d*-electron count on the metal, TMDs are classified in different phases or polymorphs (H, T, T′, distorted T′, etc.).[1,2] Different stacking orders of TMD layers give rise to different polytypes (1T, 2H, 3R, etc.). The trigonal prismatic phase is known as 1H (in monolayers, MLs) and has D_{3h} point symmetry. It is a hexagonal phase, with the chalcogens vertically aligned in the unit cell (**Figure 1**a). In the 1T octahedral phase, characterized by D_{3d} symmetry, one of the chalcogen planes glides with respect to the other (Figure 1b). It is worth noting that the top layer of chalcogens in a 1T polymorph still exhibits hexagonal symmetry.

The H and T phases are the most stable among group VI and group IV TMDs, respectively.[3] In group V TMDs (M= V, Nb, Ta), both H and T phases are found and it is even possible to induce the transition between them.[4,5] Reducing

I. Di Bernardo, J. Ripoll-Sau, C. G. Ayani, R. Miranda, A. L. Vázquez de Parga
Departamento de Física de la Materia Condensada
Universidad Autónoma de Madrid
Madrid 28049, Spain
E-mail: iolanda.dibernardo@imdea.org

I. Di Bernardo
ARC Centre of Excellence in Future Low-Energy Electronics Technologies
Monash University
Victoria 3800, Australia

I. Di Bernardo
School of Physics and Astronomy
Monash University
Victoria 3800, Australia

The ORCID identification number(s) for the author(s) of this article can be found under https://doi.org/10.1002/smll.202300262.

DOI: 10.1002/smll.202300262

I. Di Bernardo, J. Ripoll-Sau, J. A. Silva-Guillén, F. Calleja, C. G. Ayani, R. Miranda, M. Garnica, A. L. Vázquez de Parga
Instituto Madrileño de Estudios Avanzados en Nanociencia (IMDEA-Nanociencia)
Madrid 28049, Spain
E-mail: manuela.garnica@imdea.org

R. Miranda, M. Garnica, A. L. Vázquez de Parga
Instituto Nicolás Cabrera
Universidad Autónoma de Madrid
Madrid 28049, Spain

R. Miranda, A. L. Vázquez de Parga
Condensed Matter Physics Center (IFIMAC)
Universidad Autónoma de Madrid
Madrid 28049, Spain

E. Canadell
Institut de Ciència de Materials de Barcelona
ICMAB-CSIC
Campus UAB
Bellaterra 08193, Spain

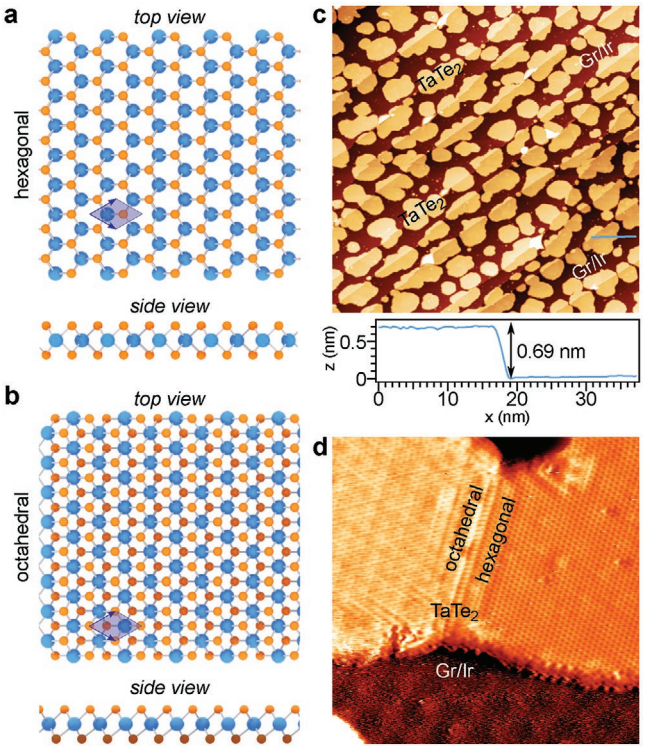

Figure 1. Ball-stick model of the hexagonal (a) and octahedral (b) polymorphs, top and side view. Blue and orange balls represent the Ta and Te atoms, respectively; in (b) the different shade of orange accounts for the two inequivalent chalcogen sites. Blue arrows enclose the shaded area corresponding to one unit cell. c) Large scale (300 nm × 300 nm) topographic image showing about 60% $TaTe_2$ monolayer (ML) coverage (bright islands) on Gr/Ir(111) (dark substrate). A line profile across an island step edge (blue line in the top panel) reveals a height of 6.9 Å. Scalebar: 50 nm; $I = 0.1$ nA; $V = 1$ V. d) Zoom-in (15 nm × 15 nm) topographic image of a $TaTe_2$ island showing two different reconstructions. To enhance features, the z signal is mixed with its derivative. $I = 0.3$ nA; $V = 0.4$ V. Sample grown at 440 K and data acquired at room temperature (RT).

the thickness down to a ML and tailoring the growth conditions (temperature, strain, substrate geometry) can result in TMD films with a polymorphic phase— and physical properties—strikingly different from the bulk one.[6,7] For example, an indirect to direct bandgap transition has been observed by thinning down 2H-MoS_2[8] and 2H-$MoSe_2$[9] to the ML; the emergence of an excitonic insulator state has been reported in ML 1T′-WTe_2;[10,11] $IrTe_2$, metallic in the bilayer, dimerizes in a distorted (2 × 1) 1T structure as a ML and undergoes a metal-to-insulator transition;[6] Ising superconductivity is observed in ML $NbSe_2$.[12]

Group V TMDs have played a significant role in the unraveling of CDW phenomena. Most of the initial studies focused on CDWs in group V sulfides and selenides, with tellurides arousing real interest only in the last couple of years. The very diffuse nature of the tellurium orbitals may cause a considerably large electron transfer from the chalcogens to the transition metal atoms,[13] leading to remarkable differences with respect to their sulfides and selenides counterparts. The absence of interlayer Te...Te interactions in the ML can result in a substantial variation of the electronic transfer compared to a multilayer system. This drove the interest to prepare and characterize ML group V transition metal ditellurides.

Bulk $TaTe_2$ is metallic[14] and exhibits a distorted 1T′ structure at room temperature (RT),[14,15] with surface Ta atoms arranged in double Ta zigzag trimer chains (see Figure S1a, Supporting Information). This peculiar structure is formed as a result of the abovementioned large Te to Ta electron transfer.[16,17] Because of the trimeric zigzag chains, each layer of 1T′-$TaTe_2$ can be thought of as a (3 × 1) reconstruction of an ideal, undistorted 1T structure. Bulk 1T′-$TaTe_2$ undergoes a structural deformation around 170 K, [18] below which the zigzag trimer chains rearrange and the periodicity along the chains becomes three times larger. Consequently, below 170 K the layers can be described as a (3 × 3) reconstruction of 1T-$TaTe_2$ (see Figure S1b, Supporting Information). The formation of a CDW at low temperatures (LTs) and the emergence of a $(\sqrt{19} \times \sqrt{19})$ periodicity (Figure S1c, Supporting Information) has also been known for quite some time.[19,20] The metallic character is kept across the transition, although anomalies in the resistivity, magnetic susceptibility, and specific heat capacity are detected.[18]

The first molecular beam epitaxy (MBE) growth of thin films of $TaTe_2$ on bilayer graphene/SiC was recently reported.[21] The authors observed a 1T phase (rather than the distorted 1T′) for thicknesses up to 8MLs, and irreversible CDW transitions in the ML as a function of the substrate annealing temperature. For high substrate temperatures and thicknesses above the ML, the most stable superstructure was found to be the $(\sqrt{19} \times \sqrt{19})$ CDW. A photoemission-based work also recently reported the formation of a 2H reconstruction on the topmost layer of a distorted 1T′-$TaTe_2$ bulk crystal.[22] These studies suggest the possibility of phase coexistence and phase tunability with thickness in $TaTe_2$, as previously reported for other TMDs on similar substrates.[7,11,23–26]

In this work, we report the growth of sub-ML $TaTe_2$ on a graphene/Ir(111) (gr/Ir(111)) substrate via MBE. The choice of gr/Ir(111) was based on its ability to be grown as a single crystal with low occurrence of defects, as well as on the minimum interaction with other TMDs, as previous works have shown.[25,26] We observe the coexistence of the two metastable 1H (trigonal prismatic) and 1T (octahedral) phases and investigate their properties via scanning tunneling microscopy (STM) and spectroscopy (STS) at RT and at 77 K. At both temperatures, the octahedral phase exhibits periodic superstructures, compatible with the ones observed in bulk crystals. The 1H phase, never reported before, undergoes a restructuring of its superperiodicity between RT and 77 K. We also demonstrate tuning of the relative phase coverage by controlling the growth conditions and extract information about the Te desorption energy from the surface by a simple adsorption–desorption model. The relative stability of the different crystallographic phases and periodicities found in the experiments are rationalized by means of first-principles density functional theory (DFT) calculations. The combination of MBE growth, *in situ* STM characterization and first-principles calculations is a powerful strategy to obtain and investigate metastable polymorphic phases with predicted new properties not present in the naturally occurring crystals.[14,27,28]

2. Results

We investigate the structure of MBE-grown $TaTe_2$ on gr/Ir(111) in the sub-ML regime. Figure 1c shows a large scale (300 nm × 300 nm) STM topographic image of $TaTe_2$ islands (bright) on gr/Ir(111) (dark) acquired at RT. The islands appear flat, slightly dendritic, and cover about 60% of the surface. A line profile across an island step edge (blue line in Figure 1c) reveals a step height of 6.9 Å, compatible with the thickness of a single TMD layer.[23,29] We can tune the $TaTe_2$ coverage by controlling growth time and elemental precursors ratio, and we observe minimal bilayer formation even at coverages as high as 80%. Figure 1d shows a close-up (15 nm × 15 nm) on the surface. Visible in the bottom part of the image is the well-known moiré pattern of graphene on Ir(111).[25] In the top part of the image, we observe a $TaTe_2$ island with two different reconstructions separated by a line defect. On both sides of the island the atomic arrangement presents a hexagonal symmetry, with the left-hand side additionally showing a superperiodic pattern. Neither side, however, shows a reconstruction compatible with the double zigzag "ribbon chain" corresponding to the distorted 1T′ phase observed on the surface of bulk $TaTe_2$.[17,30,31]

Figure 2 shows a RT high-resolution STM topographic image obtained on an island showing the most common superstructures of the octahedral phase. Other superstructures are described in Section S2 (Supporting information) and will be discussed in detail in the following. The pattern in Figure 2a closely resembles the one reported for the topmost layer of bulk 1T′-$TaTe_2$ at 77 K, [30] and was never observed before at RT. A threefold-symmetric pattern is seen in the top part of the image, while the reconstruction on the lower part exhibits a preferential symmetry axis. This pattern was ascribed to an incommensurate CDW, resulting from the competition between the hexagonal (3 × 3) and the rectangular $(3\sqrt{3}/2\times4)$ $R30°$ sharing a symmetry axis along the direction of the stripes.[30] The corresponding fast Fourier transform (FFT) pattern (Figure 2b) exhibits two distinct sets of spots corresponding to the (1 × 1) periodicity (dashed green circles) and to an incommensurate quasi-(3 × 3) (solid red circles). To verify the incommensurability of the pattern, we take a line profile across the image (black line in Figure 2a) and track the position of one in every three maxima starting from two consecutive maxima (highlighted in blue and purple, respectively) along this line. The profile is reported in Figure 2c, with the position of the maxima marked with light blue and purple dashed vertical lines. The distance between the maxima varies along the profile, confirming the incommensurability of the system. The RT evolution of this pattern as a function of the tip-sample bias is shown in Figure S2 (Supporting Information). At RT we also observe small patches of a flower-like reconstruction, similar to the one recently reported by Hwang and coworkers,[21] and a (3 × 1) reconstruction (see Figure S3, Supporting Information), both discussed below. The existence of CDWs has been reported for other ditellurides (VTe_2,[32] $TiTe_2$,[33] $NbTe_2$[34]), and demonstrated for 1T-$TaTe_2$ film thickness up to 8 ML.[21] We, therefore, tentatively attribute these superperiodicities to the presence of CDWs at RT. The average step height of the octahedral islands is 732 ± 40 pm, obtained by averaging over 40 profiles acquired with different bias voltages across different sample preparations (see Section S3, Supporting Information, for details).

Coexisting with the octahedral phase we observe a hexagonal phase shown in **Figure 3**a. The average step height of these islands is 681 ± 60 pm, consistently smaller than the one measured on the islands with the octahedral phase (see Section S3, Supporting Information, for details). The smaller step height

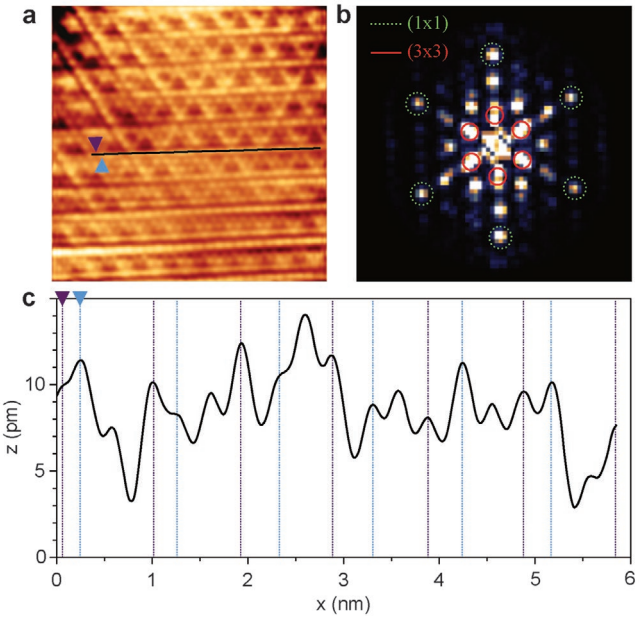

Figure 2. a) (8 nm × 8 nm) image of an octahedral area (I = 2 nA; V = − 0.5 V). b) 2D fast Fourier transform (FFT) of the image shown in panel (a). c) Line profile acquired along the black line in (a). The purple and blue triangles in panels (a) and (c) indicate the starting positions of the consecutive maxima in the line profile. c) Light blue and purple dashed lines serve as a guide to the eye to track the position of one on every three maxima, highlighting the incommensurability of the system. b) The spots corresponding to the (1 × 1) and quasi-(3 × 3) periodicities are highlighted in dashed green and solid red, respectively. All measurements were carried out at room temperature (RT).

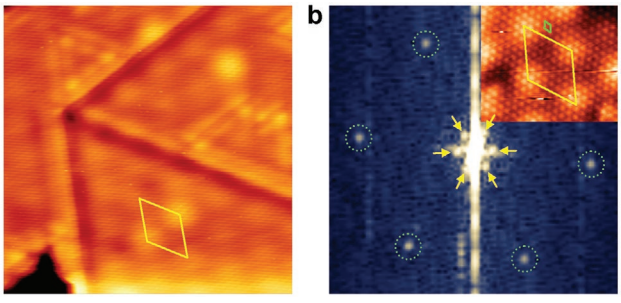

Figure 3. a) A (15 nm × 15 nm) room temperature (RT) image of a 1H area (I = 3 nA; V = 1 V). b) An (8 nm^{-1} × 8 nm^{-1}) fast Fourier transform (FFT) pattern of a (10 nm × 10 nm) atomic resolution scanning tunneling microscopy (STM) image; I = 3 nA; V = 1 V. The spots from the $TaTe_2$ atomic lattice and from the underlying gr/Ir moiré pattern are highlighted by green dotted circles and yellow arrows, respectively. The inset shows a portion of the original STM image where both periodicities are highlighted following the same color code. The gr/Ir moiré cell is also highlighted in panel (a) as a visual guide. All measurements were carried out at RT.

of the islands can be understood if it is assumed that crystallized islands in different polymorphs co-exist on the surface. In particular, the H-phase step edges are expected to be slightly lower than the octahedral ones because the partial distortion of the latter induces a buckling of the chalcogen atoms. These islands also exhibit a superlattice modulation, but its periodicity and pattern do not change as a function of tip-sample bias (Figure S4, Supporting Information). We attribute this intensity modulation to the moiré pattern of the underlying gr/Ir(111) substrate, visible through the $TaTe_2$ island. An atomically resolved STM image of the 1H island and its corresponding FFT pattern are shown in Figure 3b. Based on the analysis of this pattern we obtain a real-space periodicity of 3.3 ± 0.4 Å for the atomic lattice of $TaTe_2$, reasonably close to the expected 3.6 Å,[27] especially taking into account the fact that these are RT measurements. Taking this ideal value as a reference, the ratio between the atomic spots and that of the first-order moiré superstructure yields a real-space periodicity of 2.5 ± 0.2 nm, in perfect agreement with the known value for the gr/Ir(111) moiré.[35] Similar behavior has been reported for other TMDs layers grown on gr/Ir(111).[26] Corroborating the attribution to an H phase is the observation of mirror twin boundaries (MTBs) in this type of islands. MTBs have primarily been reported for other H-TMDs grown on hexagonal substrates,[36–39] and at the interface between octahedral and H islands.[40] MTBs form when the adlayer has a threefold symmetry (120°) while the substrate has a sixfold (60°) one: two TMD 60°-rotated domains are equivalent to two mirrored ones, and their junction will form a MTB.[39,41] The relative coverage of the H and octahedral areas ratio on the sample can be tuned as a function of substrate temperature and growth time (see Discussion section).

Figure 4 reports the different polymorphs and superperiodicities observed at 77 K on the sample prepared at 440 K under similar conditions than before. The flatter-looking areas, generally enclosed by MTBs, are attributed to the hexagonal phase, and described below. The rest is assigned to the octahedral areas, which reveal different superstructures, as seen in panels (b–d). The flower-like structure in Figure 4b, also observed at RT, has recently been attributed to the $(\sqrt{19}\times\sqrt{19})$ CDW[21] originally reported in bulk $TaTe_2$.[19,20] An alternative explanation identifies this superstructure as a chalcogen-deficient stoichiometric phase, like the one reported for Mo_5Te_8.[42] We find this pattern to be predominant for higher coverages and higher growth temperatures. This would suggest that it is the most thermodynamically stable among the superlattices for the growth parameters explored in this study. Further investigations, based on stoichiometrically accurate measurements (such as XPS or EDX, and beyond the scope of this work), are necessary to univocally establish the correct interpretation.

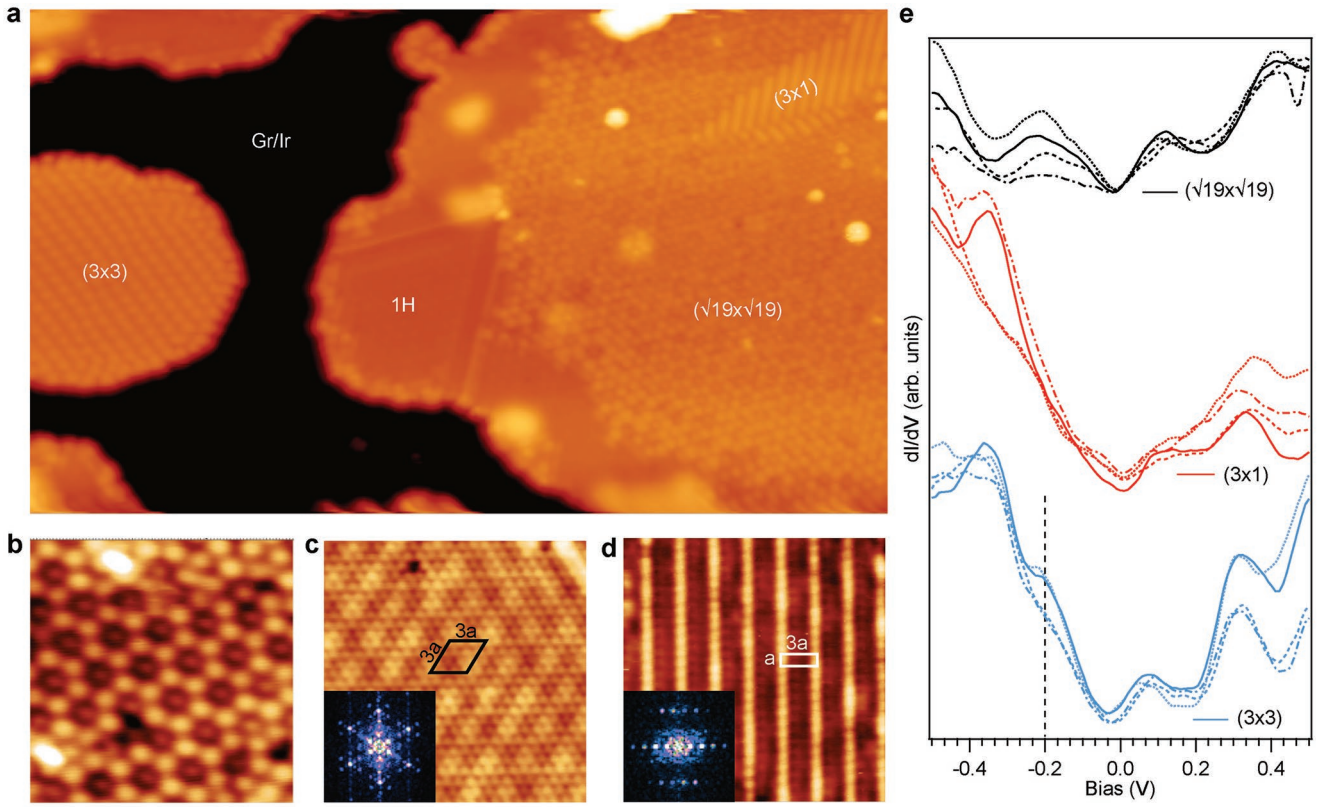

Figure 4. a) A (60 nm × 35 nm) topography showing the coexistence of two distinct phases and multiple superperiodic patterns (I = 0.3 nA; V = –1 V). Close-up micrographs of areas exhibiting reconstructions compatible with: b) $(\sqrt{19}\times\sqrt{19})$, c) (3 × 3), d) (3 × 1) superlattices. b) (8 nm × 8 nm), I = 0.1 nA, V = – 1 V. c) (7 nm × 7 nm), I = 1 nA; V = 10 mV. d) (7 nm × 7 nm), I = 1 nA; V = – 0.1 V. e) Scanning tunneling spectroscopy (STS) spectra acquired on the different periodic reconstructions. Spectra of the same color but different line styles are acquired on the same area but different spots. Sample grown at 440 K and data acquired at 77 K.

On other octahedral-phase islands (left of Figure 4a), we distinguish a (3 × 3) reconstruction (Figure 4c), appearing like a hexagonal close packed lattice of bright bumps on the large-scale images. A careful analysis of the FFT pattern of Figure 4c (inset) and Figure S7 (Supporting Information) shows an additional periodicity related to the moiré lattice of the gr/Ir substrate, similarly to what is observed for the 1H islands at RT (see Figure 3). Additionally, we observe a (3 × 1) reconstruction (Figure 4d) usually embedded within larger areas of $(\sqrt{19}\times\sqrt{19})$, with a typically fish-scale pattern, with adjacent domains rotated by 120°. Notably, a competition between the triple-axis (3 × 3) and the single axis (3 × 1) periodicities was reported to be at the origin of the "irregular" CDW observed on the surface of bulk $TaTe_2$ at 77 K[30] and theoretical calculations predict the existence of both (3 × 1) and (3 × 3) CDWs in ML 1T-$TaTe_2$.[27] While these observations would support the attribution of the (3 × 1) and (3 × 3) patterns to CDWs, based on our STM measurements it is difficult to disentangle whether the superperiodicities are to be univocally ascribed to charge modulation or an actual lattice reconstruction.

We report the STS spectra on the three differently patterned areas of panels (b–d) at 77 K in Figure 4e. We observe a series of common features, like the presence of a dip in the density of states in the proximity of the Fermi level—which does not, in any case, go to zero and open a bandgap (see Section S4, Supporting Information, for a detailed discussion). These observations point to the coexistence of multiple CDWs on the surface at the probed temperatures, rather than the conversion of one into another at given growth and annealing conditions.

The introduction of a new periodicity below a certain temperature should reflect on the band structure of the system. The phase transition at 170 K in bulk 1T′-$TaTe_2$ has recently been studied via ARPES: at LTs, a suppression of the spectral weight, associated with the formation of minigaps, has been observed at binding energies of −100 and −270 meV. Such suppression is attributed to the band folding effect induced by the formation of the (3 × 3) periodicity below 170 K. As a consequence of these dips, the DOS appears to have a peak at ≈−200 meV. The blue spectra in Figure 4e, showing STS measured on areas of our sample with (3 × 3) periodicity, show indeed a shoulder at about −200 meV (black vertical dashed line in Figure 4e). STS spectra measured on the areas with a (3 × 1) periodicity, on the other hand, do not show such feature, in good agreement with the ARPES data. The other spectral characteristics, common to all the 1T areas of the surface, can be ascribed to the shape of the band structure at the Fermi level in the T phase of $TaTe_2$.[28]

At 77 K we observe a (3 × 3) modulation on the hexagonal phase as well, as seen in **Figure 5**a,b. The enclosure within MTBs with a 60° angle between them supports the attribution to an H phase rather than a T one. Closed MTB triangular loops, like the one in Figure 5b, have been reported to originate from slightly chalcogen-deficient growth conditions.[39] The spectral weight distribution in STS data acquired on the 1H-$TaTe_2$ phase showing the (3 × 3) reconstruction (Figure 5c) is very different from that acquired on the octahedral phase (Figure 4e). The spectra reflect the metallic character of the 1H phase, with a pronounced feature at positive bias (empty states). This feature, located at ≈ 270 meV, could originate from a band edge located at the Γ point according to the calculated band

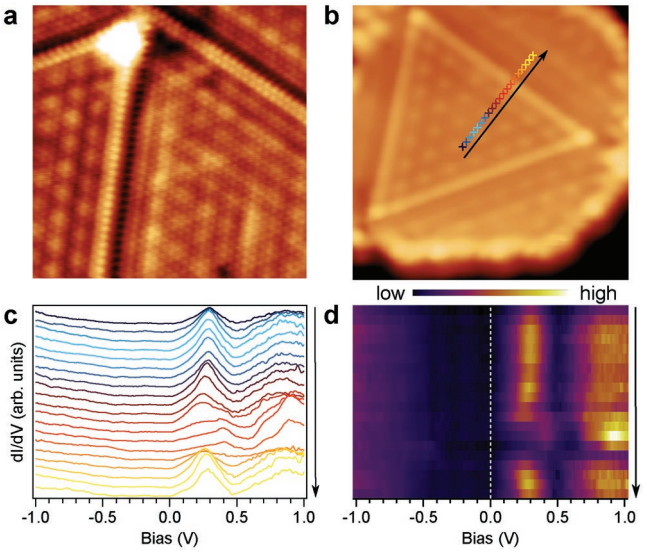

Figure 5. 1H phase characterization at 77 K. a) Atomically resolved (10 nm × 10 nm) image of a 1H area showing mirror twin boundaries (MTBs) and the (3 × 3) charge density wave (CDW). $I = 200$ pA; $V = 10$ mV. b) (6 nm × 6 nm) image showing an MTB loop. $I = 100$ pA; $V = -1$ V. c) Scanning tunneling spectroscopy (STS) spectra acquired along the line in panel (b); the spectra are color-coded and vertically offset for clarity. d) Heat-map corresponding to the spectra in panel (c).

structure,[28] like in $NbSe_2$.[43,44] We perform line-profile STS in the direction perpendicular to the MTB, presented as a stack in Figure 5c and as a heat map in Figure 5d. The black arrow in panels (b–d) points in the direction of the scan acquisition. The metallicity of the sample is preserved across the MTB, with a charge redistribution in the empty states seen in correspondence of the boundary itself.

3. Discussion

The possibility to grow $TaTe_2$ MLs in both trigonal prismatic and octahedral coordination, as well as the coexistence of different CDW patterns, are striking and call for a rationalization. We thus carried out first-principles DFT calculations on different phases of $TaTe_2$ to estimate their stabilities (see **Tables 1** and **2**).

The reliability of the calculations was tested by first looking at $TaTe_2$ bulk. The ground state of bulk $TaTe_2$ is found to be the (3 × 3) phase, with the (3 × 1) only 6 meV f. u.$^{-1}$ higher in energy. By contrast, the two hexagonal 1T and 2H phases are found at considerably higher energies (160 and 128 meV f.u.$^{-1}$, respectively) (see Table 1). These results are in excellent agreement with the experimental observation that bulk $TaTe_2$ crystals

Table 1. Relative energies, ΔE (meV f. u.$^{-1}$) for different $TaTe_2$ phases in bulk.

	Octahedral			Hexagonal
Phase	3 × 3	3 × 1	1T	2H
ΔE	0	+6	+160	+128

Table 2. Relative energies, ΔE (meV f. u.$^{-1}$) for different ML-$TaTe_2$ phases.

	Octahedral						Hexagonal	
Phase	3 × 3	3 × 1	$\sqrt{7}\times\sqrt{7}$	$\sqrt{13}\times\sqrt{13}$	$\sqrt{19}\times\sqrt{19}$	1T	1H	3 × 3
ΔE	0	+12	+82	+17	+50	+131	+122	+100.

exist only in the distorted (3 × 1) phase at RT and distort to the (3 × 3) one at LT, lending credit to the calculations for the ML.

We considered self-standing MLs of the (3 × 3) and (3 × 1) phases as well as other possible superstructures of the 1T and 1H phases: $(\sqrt{7}\times\sqrt{7})$, $(\sqrt{13}\times\sqrt{13})$, and $(\sqrt{19}\times\sqrt{19})$ for 1T; (3 × 3) for 1H. Overall, the more stable phase is found to be the (3 × 3), followed by the (3 × 1) at a relatively small energy difference of 12 meV f. u.$^{-1}$. The other superperiodicities are all found at higher energies (see Table 2). The 1T and 1H phases remain considerably higher in energy in the ML regime (see Table 2).

The theoretical results provide some useful hints concerning the stability of different ML $TaTe_2$ phases:

(i) The large stabilization of 1T vs. 1H when going from bulk to ML shows that interlayer interactions have an important differential effect in stabilizing certain phases of $TaTe_2$.
(ii) While at RT bulk TaS_2 and $TaSe_2$ are found in 1T/2H forms, $TaTe_2$ is found in the (3 × 1) octahedral structure. Our calculations suggest that the strong preference for the octahedral coordination is due to a strong driving force toward a (3 × 1) type clustering, leading to short Ta–Ta bonds in both bulk and ML. Ta–Ta clustering in H type layers toward a (3 × 3) CDW provides a stabilization which is 5–6 times weaker.
(iii) Comparing the results in Tables 1 and 2 we observe that, when the interlayer Te...Te interactions are quenched (in the ML), the stabilization of the (3 × 1) phase with respect to the 1T is weaker. This supports previous suggestions that the Te to Ta electron transfer, which is maximized in the bulk, is the major factor behind the distortion toward the (3 × 1) structure.[16,17]
(iv) The suppression of the interlayer Te...Te interactions in the ML increases the stability of the (3 × 3) phase with respect to the (3 × 1). This means that the interlayer Te...Te interactions are not the only factor to consider in understanding the relative stability of these phases: the interlayer Te...Te interactions favor the distortion from 1T toward the (3 × 1) phase, while the intralayer Te...Te interactions favor the subsequent distortion toward the (3 × 3) phase. In other words, the decompression effect of removing adjacent layers is also responsible for changes in the intralayer Te... Te interactions.
(v) While the 1T phase is preferred over the 1H in ML VTe_2 and ML $NbTe_2$, such preference is reversed for ML $TaTe_2$ (see **Table 3**). In any way, this means that the metal-to-metal interactions also influence in a nonnegligible way the stability of the $TaTe_2$ phases.
(vi) A recent MBE study[21] supports our conclusion that a phase compatible with a $(\sqrt{19}\times\sqrt{19})$ CDW could be prepared under certain conditions. As shown in Table 2, all $(\sqrt{m}\times\sqrt{m})$ superstructures considered here have energy stabilities in-between those of the octahedral (3 × 3) and 1H phases observed in the present work. This suggests that ML phases like the $(\sqrt{7}\times\sqrt{7})$ and $(\sqrt{13}\times\sqrt{13})$ may also be prepared via MBE, by appropriately tuning the working conditions.

Table 3. Relative energies between the 1H (hexagonal) and 1T (octahedral) phases, $\Delta E_{(1H\text{-}1T)}$ (meV f. u.$^{-1}$) for different ML MTe_2 compounds.

Element (M)	V	Nb	Ta
$\Delta E_{1H\text{-}1T}$	+100	+6	−9

Taken together, these observations suggest that there is a delicate trade between Te...Te and Ta...Ta interactions, which govern the stability of different $TaTe_2$ ML phases. MBE may provide a very useful approach to prepare $TaTe_2$ phases differing by as much as ≈100 meV f. u.$^{-1}$ in stability using appropriate growth conditions.

We now discuss phase tunability. Usually, phase engineering of TMDs is achieved by changing the occupation of the *d* orbitals of the transition metal[45] (for example by alkali/salt intercalation) or by applying strain. Tuning of the growth temperature (therefore, of the adatom mobility on the substrate) and of the metal-chalcogen ratio have also been reported as efficient techniques to control the morphology and grain size in transition metal diselenides[29] and ditellurides.[25] We can phase-engineer ML $TaTe_2$ by tuning the growth temperature. Considering all superperiodicities, we observe a larger octahedral:hexagonal area ratio for higher growth temperatures (**Figure 6** and Figure S6, Supporting Information) and longer growth times, in line with theoretical prediction that the octahedral phase is the most stable for the ML. Note that our experiments are apparently contradicting the results of Hwang et al.,[21] who observe only the 1T phase in their work. The authors used a similarly inert substrate (bilayer graphene on SiC, compared to our graphene on iridium) and reported a Ta:Te ratio during growth between 1: 20 and 1: 30, well within our 1:6–1:40 range. The lowest growth temperature reported in

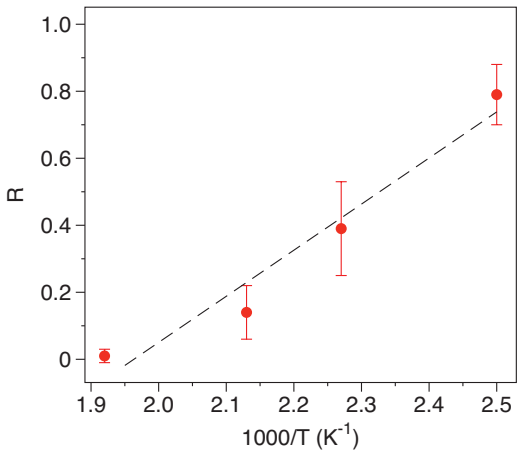

Figure 6. Phase tunability with temperature. Hexagonal:octahedral phase area ratio (*R*) as a function of the inverse of growth temperature. Data extracted from scanning tunneling microscopy (STM) measurements acquired at room temperature (RT).

their work[21] however, is 535 K, larger than the highest growth temperature reported in this work (510 K). Extrapolating from the plot in Figure 6, at temperatures higher than 510 K the only phase expected is the 1T, coherently with the recent report. In the temperature range we investigate, the relative coverage of the octahedral (3 × 3) phase can be tuned while the coverage of the (3 × 1) and the ($\sqrt{19}\times\sqrt{19}$) superstructures remain more or less constant.

The temperature-dependent 1H → 1T phase transition can be used to extract information about the tellurium desorption energy from the substrate surface, following the approach of Chen and coworkers.[46] We define the H:T ratio as $R = \frac{A_H}{A_T + A_H}$, calculated from the relative phase coverage for different growth temperatures estimated via STM image processing. We then plot R against the inverse of growth temperature and observe that the formation of the 1H phase (high R values) is favored at lower growth temperatures. The 1H phase is therefore promoted when tellurium adatoms linger on the surface for longer before being incorporated in an island or being desorbed. From the plot in Figure 6, R follows an Arrhenius model: $R \propto e^{E/k_B T} = E/k_B T$ where E is the activation energy for the reaction. This activation energy can be related to the rate of adsorption–desorption of Te for the surface. In first order adsorption–desorption kinetics, neglecting the incorporation in islands, the rate of change of the adsorbate coverage θ, proportional to R, is $\frac{d\theta}{dt} = F k_\alpha - \theta k_d$ where F is the flux and the $k_{\alpha/d}$ are the adsorption–desorption coefficients. At steady state $\frac{d\theta}{dt} = 0$, so $\theta = F\frac{k_\alpha}{k_d}$. As $R \propto \theta$, by doing a linear fit on the plot we can extract an activation energy of 0.12 eV, value linked to the energy barrier necessary to desorb Te from the surface. This value is in good agreement with the 0.17 eV calculated to be necessary for desorption of Te from HOPG.[46] This plot demonstrates the important role of the growth temperature for tuning the phase of TMDs ML.

4. Conclusion

We have discovered the possibility of growing, via MBE, MLs of the hexagonal and octahedral polymorphs of the TMD $TaTe_2$. These two metastable phases are not observed in bulk crystals. STM measurements reveal that the octahedral phase exhibits multiple coexisting—rather than mutually exclusive—CDW patterns at RT and 77 K. STM and STS measurements also highlight the existence of a metallic 1H phase, never reported before, which supports the formation of CDW at cryogenic temperatures. Theoretical results demonstrate that a subtle trade between Te...Te (both inter- and intralayer) and Ta...Ta interactions governs the stability of the different $TaTe_2$ ML phases. Tuning the relative coverage of one phase over the other is simply obtained by tuning of the growth temperature. Our combined experimental–theoretical study demonstrates that MBE is a simple but reliable method to obtain bulk-unstable phases and lateral homojunctions, as phases differing in stability by as much as ≈100 meV f. u.$^{-1}$ can be prepared using this technique. Our synthesis method enables to access and study a very rich landscape of different phases and lattice supermodulations, never reported before for any other transition metal dichalcogenide.

5. Experimental Section

MBE Growth: The gr/Ir(111) surface was prepared by three cycles of Ar+ ion sputtering at 1 keV (pressure 3.6 × 10^{-6} Torr) followed by a flash annealing at 1600 K. After last cycle, the surface was exposed to 33 L of ethylene while keeping the sample at 1440 K. This well-established procedure[25] results is an atomically flat Ir(111) surface almost completely covered by a single layer of graphene. $TaTe_2$ growth was carried out on the gr/Ir(111) substrate by coevaporating elemental Ta and Te from an e-beam (applied voltage = 1 kV, flux = 12/24 nA) and a Knudsen cell ($T = 600K$), respectively. The flux ratio between elemental components was estimated by deposition of each of them individually on the substrate. The growth temperature used in our experiments has been 440 K, except for the phase engineering experiments in which the temperature has been ranged between 400 and 510 K. The film growth rate at 440 K is estimated to be about 0.6 ML h^{-1} by analyzing substrate coverage via STM.

STM-STS Measurements: The morphology and electronic structure of the samples were measured using either a RT STM system, directly connected to the preparation chamber, or LT system, where the STM head is in thermal equilibrium with a liquid nitrogen bath (base temperature = 77 K). For STS measurements a lock-in amplifier was used, where the modulation frequency was 721 Hz.

First-Principles Calculations: Numerical calculations were carried out using DFT[47,48] as implemented in the SIESTA code.[49–51] The generalized gradient approximation (GGA), specifically, the revised Perdew–Burke–Ernzerhof functional for solids and surfaces PBEsol.[52] To describe the core electrons we used norm-conserving scalar relativistic pseudopotentials with non-linear core corrections.[53,54] The valence electrons were described with a split-valence double-ζ basis set including polarization functions.[55] The energy cutoff of the real space integration mesh was set to 500 Ry. To build the charge density (and, from this, obtain the DFT total energy and atomic forces), the reciprocal space was sampled with the Monkhorst–Pack scheme.[56] The number of k-points was optimized for two structures for both the bulk and single-layer systems, the 1T and 1T′, resulting in grids of (39 × 39 × 7) and (10 × 42 × 14) for bulk and (39 × 39 × 1) and (10 × 42 × 1) for the single-layer case. For the other phases the grid was scaled accordingly. Both the lattice parameters and the atomic positions were optimized. The forces acting on the atoms were smaller than 0.04 eVAng^{-1}.

Supporting Information

Supporting Information is available from the Wiley Online Library or from the author.

Acknowledgements

This work was supported by the Spanish Ministry of Science and Innovation (Grant nos. PID2021-123776NB-C21, PGC2018-096955-B-C44, and PID2021-128011NB-I00) and the Comunidad de Madrid (Project S2018/NMT-4511, NMAT2D). IMDEA Nanociencia and IFIMAC acknowledge financial support from the Spanish Ministry of Science and Innovation 'Severo Ochoa' (Grant CEX2020-001039-S) and 'María de Maeztu' (Grant CEX2018-000805-M) Programme for Centres of Excellence in R&D, respectively. Financial support through the (MAD2D-CM)-MRR MATERIALES AVANZADOS-IMDEA-NC and (MAD2D-CM) MRR MATERIALES AVANZADOS-UAM2 is acknowledged. M.G. has received financial support through the "Ramón y Cajal" Fellowship program (RYC2020-029317-I). I.D.B. acknowledges support from the

Maria de Zambrano fellowship program and the MSCA Program (101063547-GAP-101063547), as well as from the FLEET Centre of Excellence, ARC Grant No. CE170100039. E.C. acknowledges support of the Spanish MICIU through the Severo Ochoa FUNFUTURE (CEX2019-000917-S) Excellence Centre distinction and Generalitat de Catalunya (2021SGR01519). J.A.S.G. thankfully acknowledges the computer resources at Marigold and the technical support provided by SCAYLE (RES-FI-2020-2-0040) as well as the computer resources of CCCUAM.

Conflict of Interest

The authors declare no conflict of interest.

Author Contributions

I.D.B. and J.R.-S. contributed equally to this work. M.G., I.D.B. and J.A.S.G. conceived the original idea. J.A.S.G. and E.C. developed the theory and performed the calculations. J.R.S., I.D.B. and M.G. carried out the experiment and conducted the analysis with the support of C.G.A., F.C., A.L.V.d.P. and R.M. I.D.B. and A.L.V.d.P. wrote the manuscript with support of J.A.S.G., E.C. and M.G. All authors have given approval to the final version of the manuscript.

Data Availability Statement

The data that support the findings of this study are available from the corresponding author upon reasonable request.

Keywords

density functional theory, molecular beam epitaxy (MBE), scanning tunneling microscopy (STM), $TaTe_2$, transition metal dichalcogenides (TMDs)

Received: January 10, 2023
Revised: March 9, 2023
Published online:

[1] X. Yin, C. S. Tang, Y. Zheng, J. Gao, J. Wu, H. Zhang, M. Chhowalla, W. Chen, A. T. S. Wee, *Chem. Soc. Rev.* **2021**, *50*, 10087.
[2] S. Manzeli, D. Ovchinnikov, D. Pasquier, O. V. Yazyev, A. Kis, *Nat. Rev. Mater.* **2017**, *2*, 17033.
[3] Z. Wang, Y. Y. Sun, I. Abdelwahab, L. Cao, W. Yu, H. Ju, J. Zhu, W. Fu, L. Chu, H. Xu, K. P. Loh, *ACS Nano* **2018**, *12*, 12619.
[4] S. Wang, D. Zhang, B. Li, C. Zhang, Z. Du, H. Yin, X. Bi, S. Yang, *Adv. Energy Mater.* **2018**, *8*, 1801345.
[5] F. Bischoff, W. Auwärter, J. V. Barth, A. Schiffrin, M. Fuhrer, B. Weber, *Chem. Mater.* **2017**, *29*, 9907.
[6] J. Hwang, K. Kim, C. Zhang, T. Zhu, C. Herbig, S. Kim, B. Kim, Y. Zhong, M. Salah, M. M. El-Desoky, C. Hwang, Z.-X. X. Shen, M. F. Crommie, S.-K. K. Mo, *Nat. Commun.* **2022**, *13*, 906.
[7] P. M. Coelho, K. Lasek, K. Nguyen Cong, J. Li, W. Niu, W. Liu, I. I. Oleynik, M. Batzill, *J. Phys. Chem. Lett.* **2019**, *10*, 4987.
[8] A. Splendiani, L. Sun, Y. Zhang, T. Li, J. Kim, C.-Y. Chim, G. Galli, F. Wang, *Nano Lett.* **2010**, *10*, 1271.
[9] Y. Zhang, T.-R. Chang, B. Zhou, Y.-T. Cui, H. Yan, Z. Liu, F. Schmitt, J. Lee, R. Moore, Y. Chen, H. Lin, H.-T. Jeng, S.-K. Mo, Z. Hussain, A. Bansil, Z.-X. Shen, *Nat. Nanotechnol.* **2014**, *9*, 111.
[10] B. Sun, W. Zhao, T. Palomaki, Z. Fei, E. Runburg, P. Malinowski, X. Huang, J. Cenker, Y. T. Cui, J. H. Chu, X. Xu, S. S. Ataei, D. Varsano, M. Palummo, E. Molinari, M. Rontani, D. H. Cobden, *Nat. Phys.* **2022**, *18*, 94.
[11] Y. Jia, P. Wang, C. L. Chiu, Z. Song, G. Yu, B. Jäck, S. Lei, S. Klemenz, F. A. Cevallos, M. Onyszczak, N. Fishchenko, X. Liu, G. Farahi, F. Xie, Y. Xu, K. Watanabe, T. Taniguchi, B. A. Bernevig, R. J. Cava, L. M. Schoop, A. Yazdani, S. Wu, *Nat. Phys.* **2022**, *18*, 87.
[12] X. Xi, Z. Wang, W. Zhao, J. H. Park, K. T. Law, H. Berger, L. Forró, J. Shan, K. F. Mak, *Nat. Phys.* **2016**, *12*, 139.
[13] E. Canadell, S. Jobic, R. Brec, J. Rouxel, M. H. Whangbo, *J. Solid State Chem.* **1992**, *99*, 189.
[14] J. Li, B. Zhao, P. Chen, R. Wu, B. Li, Q. Xia, G. Guo, J. Luo, K. Zang, Z. Zhang, H. Ma, G. Sun, X. Duan, X. Duan, *Adv. Mater.* **2018**, *30*, 1801043.
[15] B. E. Brown, *Acta Crystallogr.* **1966**, *20*, 264.
[16] M. H. Whangbo, E. Canadell, *J. Am. Chem. Soc.* **1992**, *114*, 9587.
[17] C. Chen, H. S. Kim, A. S. Admasu, S. W. Cheong, K. Haule, D. Vanderbilt, W. Wu, *Phys. Rev. B* **2018**, *98*, 195423.
[18] T. Sörgel, J. Nuss, U. Wedig, R. K. Kremer, M. Jansen, *Mater. Res. Bull.* **2006**, *41*, 987.
[19] J. van Landuyt, G. A. Wiegers, S. Amelinckx, *Phys. Status Solidi* **1978**, *46*, 479.
[20] J. van Landuyt, G. van Tendeloo, S. Amelinckx, *Phys. Status Solidi* **1974**, *26*, 585.
[21] J. Hwang, Y. Jin, C. Zhang, T. Zhu, K. Kim, Y. Zhong, J.-E. Lee, Z. Shen, Y. Chen, W. Ruan, H. Ryu, C. Hwang, J. Lee, M. F. Crommie, S.-K. Mo, Z.-X. Shen, *Adv. Mater.* **2022**, *34*, 2204579.
[22] I. Kar, K. Dolui, L. Harnagea, Y. Kushnirenko, G. Shipunov, N. C. Plumb, M. Shi, B. Büchner, S. Thirupathaiah, *J. Phys. Chem. C* **2021**, *125*, 1150.
[23] R. Chua, J. Yang, X. He, X. Yu, W. Yu, F. Bussolotti, P. K. J. Wong, K. P. Loh, M. B. H. Breese, K. E. J. Goh, Y. L. Huang, A. T. S. Wee, *Adv. Mater.* **2020**, *32*, 2000693.
[24] S. Cheng, L. Yang, J. Li, Z. Liu, W. Zhang, H. Chang, *CrystEngComm* **2017**, *19*, 1045.
[25] J. Ripoll-Sau, F. Calleja, P. Casado Aguilar, I. M. Ibarburu, A. L. Vázquez de Parga, R. Miranda, M. Garnica, *Nanoscale* **2022**, *14*, 10880.
[26] J. Hall, B. Pielić, C. Murray, W. Jolie, T. Wekking, C. Busse, M. Kralj, T. Michely, *2D Mater.* **2018**, *5*, 025005.
[27] D. C. Miller, S. D. Mahanti, P. M. Duxbury, *Phys. Rev. B* **2018**, *97*, 045133.
[28] N. Guo, X. Fan, Z. Chen, Z. Luo, Y. Hu, Y. An, D. Yang, S. Ma, *Comput. Mater. Sci.* **2020**, *176*, 109540.
[29] A. Rajan, K. Underwood, F. Mazzola, P. D. C. C. King, *Phys. Rev. Mater.* **2020**, *4*, 014003.
[30] J. Feng, A. Tan, S. Wagner, J. Liu, Z. Mao, X. Ke, P. Zhang, *Appl. Phys. Lett.* **2016**, *109*, 021901.
[31] I. El Baggari, N. Sivadas, G. M. Stiehl, J. Waelder, D. C. Ralph, C. J. Fennie, L. F. Kourkoutis, *Phys. Rev. Lett.* **2020**, *125*, 165302.
[32] D. Won, D. H. Kiem, H. Cho, D. Kim, Y. Kim, M. Y. Jeong, C. Seo, J. Kim, J.-G. Park, M. J. Han, H. Yang, S. Cho, *Adv. Mater.* **2020**, *32*, 1906578.
[33] S. Fragkos, R. Sant, C. Alvarez, A. Bosak, P. Tsipas, D. Tsoutsou, H. Okuno, G. Renaud, A. Dimoulas, *Adv. Mater. Interfaces* **2019**, *6*, 1801850.
[34] K. Zhang, N. Zou, Y. Ren, J. Wu, C. Si, W. Duan, *Adv. Funct. Mater.* **2022**, *32*, 2111675.
[35] J. Coraux, A. T. N'Diaye, M. Engler, C. Busse, D. Wall, N. Buckanie, F. J. Meyer zu Heringdorf, R. van Gastel, B. Poelsema, T. Michely, *New J. Phys.* **2009**, *11*, 023006.
[36] B. Wang, Y. Xia, J. Zhang, H.-P. Komsa, M. Xie, Y. Peng, C. Jin, *Nano Res.* **2020**, *13*, 1889.

[37] H. Liu, L. Jiao, F. Yang, Y. Cai, X. Wu, W. Ho, C. Gao, J. Jia, N. Wang, H. Fan, W. Yao, M. Xie, *Phys. Rev. Lett.* **2014**, *113*, 66105.
[38] O. Lehtinen, H.-P. Komsa, A. Pulkin, M. B. Whitwick, M.-W. Chen, T. Lehnert, M. J. Mohn, O. V. Yazyev, A. Kis, U. Kaiser, A. V. Krasheninnikov, *ACS Nano* **2015**, *9*, 3274.
[39] M. Batzill, *J. Phys.: Condens. Matter* **2018**, *30*, 493001.
[40] Y. C. Lin, D. O. Dumcenco, Y.-S. Huang, K. Suenaga, *Nat. Nanotechnol.* **2014**, *9*, 391.
[41] K. Lasek, J. Li, S. Kolekar, P. M. Coelho, L. Guo, M. Zhang, Z. Wang, M. Batzill, *Surf. Sci. Rep.* **2021**, *76*, 100523.
[42] J. Zhang, Y. Xia, B. Wang, Y. Jin, H. Tian, W. kin Ho, H. Xu, C. Jin, M. Xie, *2D Mater.* **2020**, *8*, 015006.
[43] M. M. Ugeda, A. J. Bradley, Y. Zhang, S. Onishi, Y. Chen, W. Ruan, C. Ojeda-Aristizabal, H. Ryu, M. T. Edmonds, H.-Z. Tsai, A. Riss, S.-K. Mo, D. Lee, A. Zettl, Z. Hussain, Z.-X. Shen, M. F. Crommie, *Nat. Phys.* **2016**, *12*, 92.
[44] J. Á. Silva-Guillén, P. Ordejón, F. Guinea, E. Canadell, *2D Mater.* **2016**, *3*, 035028.
[45] D. Voiry, A. Mohite, M. Chhowalla, *Chem. Soc. Rev.* **2015**, *44*, 2702.
[46] J. Chen, G. Wang, Y. Tang, H. Tian, J. Xu, X. Dai, H. Xu, J. Jia, W. Ho, M. Xie, *ACS Nano* **2017**, *11*, 3282.
[47] P. Hohenberg, W. Kohn, *Phys. Rev.* **1964**, *136*, B864.
[48] W. Kohn, L. J. Sham, *Phys. Rev.* **1965**, *140*, A1133.
[49] J. M. Soler, E. Artacho, J. D. Gale, A. García, J. Junquera, P. Ordejón, D. Sánchez-Portal, *J. Phys.: Condens. Matter* **2002**, *14*, 2745.
[50] E. Artacho, E. Anglada, O. Diéguez, J. D. Gale, A. García, J. Junquera, R. M. Martin, P. Ordejón, J. M. Pruneda, D. Sánchez-Portal, J. M. Soler, *J. Phys.: Condens. Matter* **2008**, *20*, 064208.
[51] A. García, N. Papior, A. Akhtar, E. Artacho, V. Blum, E. Bosoni, P. Brandimarte, M. Brandbyge, J. I. Cerdá, F. Corsetti, R. Cuadrado, V. Dikan, J. Ferrer, J. Gale, P. García-Fernández, V. M. García-Suárez, S. García, G. Huhs, S. Illera, R. Korytár, P. Koval, I. Lebedeva, L. Lin, P. López-Tarifa, S. G. Mayo, S. Mohr, P. Ordejón, A. Postnikov, Y. Pouillon, M. Pruneda, et al., *J. Chem. Phys.* **2020**, *152*, 204108.
[52] J. P. Perdew, A. Ruzsinszky, G. I. Csonka, O. A. Vydrov, G. E. Scuseria, L. A. Constantin, X. Zhou, K. Burke, *Phys. Rev. Lett.* **2008**, *100*, 136406.
[53] A. García, M. J. Verstraete, Y. Pouillon, J. Junquera, *Comput. Phys. Commun.* **2018**, *227*, 51.
[54] M. J. van Setten, M. Giantomassi, E. Bousquet, M. J. Verstraete, D. R. Hamann, X. Gonze, G. M. Rignanese, *Comput. Phys. Commun.* **2018**, *226*, 39.
[55] E. Artacho, D. Sánchez-Portal, P. Ordejón, A. García, J. M. Soler, *Phys. Status Solidi B* **1999**, *215*, 809.
[56] H. J. Monkhorst, J. D. Pack, *Phys. Rev. B* **1976**, *13*, 5188.